Split-ring resonator coupling-induced tunable acoustic second-order topological insulators

Chen Chen, Tianning Chen, Wei Ding, Xinhai Xiang, Feiran Mao, and Jian Zhu *
School of Mechanical Engineering and State Key Laboratory of Strength & Vibration of Mechanical Structures, Xi'an Jiaotong University, Xi'an, Shaanxi 710049, Peoples Republic of China

(Received 11 November 2021; accepted 9 June 2022; published 5 July 2022)

The recent higher-order topological insulators (HOTIs) encoded with the tight-binding model (TBM) have been demonstrated beyond traditional bulk-edge correspondence, which shows the exotic capability of sound manipulation. However, the current waveguide resonator model with weak tunability in hopping controls has been used as the most common method to construct the TBM directly in a realistic acoustic system. Here, we present another carrier and methodology to realize the TBM based on split-ring resonators (SRRs) coupling in a realistic physical platform and construct a second-order topological insulator (SOTI) based on it, where the hopping and frequencies of the topological corner states can be easily tuned by adjusting the coupling strength of the SRRs. Numerical analysis and experimental measurement demonstrated zero-dimensional topological corner states in this acoustic resonant system. The findings provide a more flexible method for tunable acoustic HOTIs realization.

DOI: 10.1103/PhysRevB.106.045403

I. INTRODUCTION

As a rising topological materials, higher-order topological insulators (HOTIs) have consumed the world's attention recently [1–4]. Different from the conventional topological insulators, which support topologically protected states along boundaries with one dimension lower than that of the bulk, HOTIs host the topological corner states in a two-dimensional (2D) or three-dimensional (3D) system, which obey the generalized bulk-edge correspondence principle. After the first theoretical prediction of HOTIs [1,2], quadrupole topological insulators were rapidly demonstrated in some real physical platforms, such as mechanics [5], electromagnetics [6], photonics [7,8] and acoustics [9], based on the quantized quadrupole momentum. Then, the Wannier-type second-order topological insulators (SOTIs) were predicted and demonstrated in a kagome lattice [10–13] and a square lattice [14–19] characterized with quantized dipole momentum. In addition, other SOTIs were also presented based on crystalline symmetries [20,21], valley degree of freedom [22], or Dirac vortices [23].

In particular, the tight-binding model (TBM) [24–26] as a key to obtain the system's Hamiltonian plays a vital role in the developing process of HOTIs, where controlling hopping between neighboring lattice sites is very crucial to construct HOTIs. In photonics, hopping controls for HOTIs can be easily realized experimentally by changing the distance between neighboring dielectric rods [27,28]. But in an acoustic system, this easy hopping–control strategy can only be available when the acoustic impedance of the scattering rods is lower than that of the air yet without experimental demonstration [29,30]. Therefore, the waveguide resonator model (WRM) was used to be an analogy of the TBM in the realistic system of acoustics, but with limited degrees of freedom in adjusting the hopping [31–34]. Thus, it is essential to find another carrier, with a more flexible method of adjusting the hopping, to construct the TBM in a realistic physical platform.

Here, the sonic crystal (SC) consisting of split-ring resonators (SRRs) [35–42] is demonstrated as an analogy of the TBM. The coupling of SRRs plays a key role in flexible hopping manipulation, which can be used to realize acoustic HOTIs. Different from the previous WRM-based acoustic HOTIs, the TBM based on SRRs can control the hopping by changing the split's direction of the unit, and the working frequency can be tuned by changing the distance of neighboring SRRs. Furthermore, the zero Berry curvature and quantized dipole momentum are calculated to verify the effective analogy between the resonant SC and the TBM. The topological corner states are demonstrated experimentally by constructing a superstructure composed of two topologically distinct SCs forming box-shaped boundaries.

II. ACOUSTIC TOPOLOGICAL MODEL COMPOSED OF SRRs

The square-lattice model used to construct 2D SOTIs is plotted in Fig. 1(a) and the unit cell is marked by the black dashed square with lattice constant $a = 30$ mm. The unit cell is formed by arraying one SRR (outer radius $R = 5$ mm, inner radius $r = 3.5$ mm, and width of the split $t = 3$ mm) circling the center of the unit cell every 90°, which makes this SC own C_4 symmetry. These four SRRs are positioned on the diagonal lines of the unit cell, and the distance between the SRRs with the center can be expressed as $D = \sqrt{2} \times (0.25a + \Delta d)$. The direction of the SRRs can be denoted as α. Thus, the SC can be described with Δd and α. For example, when $\alpha = 45^\circ$ and $\Delta d = -1.5$ mm, the SC can be defined as $(45, -1.5)$.

*jianzhuxj@xjtu.edu.cn

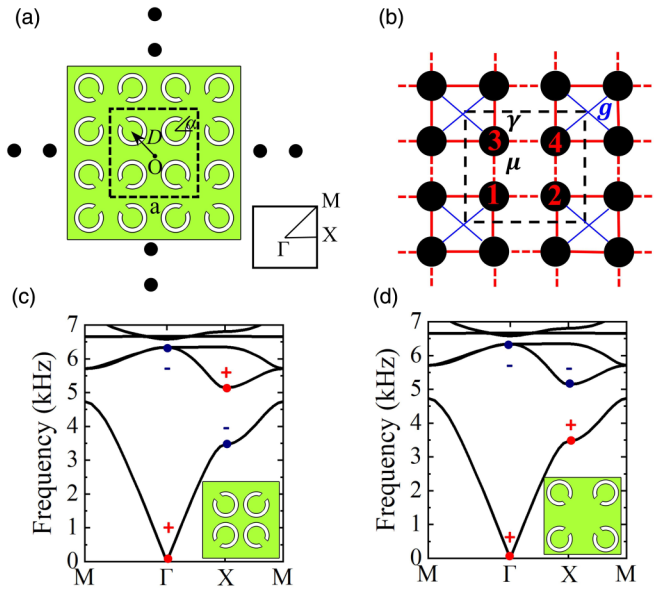

FIG. 1. Acoustic model and corresponding band structures. (a) Schematic of the square-lattice SC with the unit cell surrounded by the black dashed box. Inset: The first Brillouin zone. (b) The corresponding 2D acoustic SSH model. Band structure of nontrivial SC (45, −1.5) (c) and trivial SC (−135, 1.5) (d). The +/− signs indicate the odd and even modes at the high-symmetry points, respectively. Insets: The corresponding unit cell.

This type of SC can be approximated by a 2D Su-Schrieffer-Heeger (SSH) model [43] considering the next-nearest neighbor (NNN) coupling [Fig. 1(b)], where γ is the intercell hopping, μ is the intracell hopping, and g is the NNN coupling. The Hamiltonian in momentum space of the 2D SSH model can be described as [17]

$$H(k) = (-1)^* \begin{bmatrix} 0 & h_{12} & h_{13} & h_{14} \\ h_{12}^* & 0 & h_{23} & h_{24} \\ h_{13}^* & h_{23}^* & 0 & h_{34} \\ h_{14}^* & h_{24}^* & h_{34}^* & 0 \end{bmatrix}, \tag{1}$$

where $h_{12} = h_{34} = \mu + \gamma \exp(-ik_x)$, $h_{13} = h_{24} = \mu + \gamma \exp(-ik_y)$, $h_{14} = g\exp(-ik_x - ik_y)$, and $h_{23} = g\exp(ik_x - ik_y)$. The atomic sites in the unit cell are numbered from 1 to 4, as shown in Fig. 1(b).

In a realistic SC, μ, γ, and g are related to Δd and α of the SRR. The bulk dispersions of two different SCs defined as (45, −1.5) and (−135, 1.5) are demonstrated in Fig. 1(c) and (1d), respectively, and are calculated using an eigenfrequency analysis in the "Acoustics" module of COMSOL Multiphysics software and are very similar to the band structures calculated using the tight-binding Hamiltonian in Eq. (1) with $\mu \neq \gamma$, $g \neq 0$ (see Supplemental Material Note S1 [44]). And one absolute band gap emerges from 4735 Hz to 5141 Hz. Although these two types of SCs cannot be distinguished by band structures alone, they own different topological invariants of the first band gap. Because of the special point group symmetry of this acoustic system, the bulk polarization $\boldsymbol{P}$, the corresponding topological invariant, can be obtained from the parities of the eigenstates (see Supplemental Material Note S2 [44]) at the high-symmetry points in the first Brillouin Zone [see the inset in Fig. 1(a)] [45]:

$$P_m = \frac{1}{2}\left(\sum q_m^n \bmod 2\right),\ (-1)^{q_m^n} = \frac{\eta_n(X_m)}{\eta_n(\Gamma)}, \tag{2}$$

where the summation is carried over all the occupied bands below the first band gap, η_n denotes the parity associated with π rotation of the nth-band eigenstates at the high-symmetry point, and m stands for the direction of x or y. Here, $P_x = P_y$ because of the symmetry of this acoustic system. From the parities labeled in Fig. 1(c) and 1(d), for SC (45, −1.5), we can obtain $\boldsymbol{P} = (1/2, 1/2)$, indicating it is nontrivial; for SC (−135, 1.5), $\boldsymbol{P} = (0, 0)$, indicating it is trivial. To verify further the effective analog between the acoustic model with the 2D SSH model, we numerically calculate the Berry curvature and Wannier centers of the lowest band. The Berry curvature can be defined as

$$\Omega = \nabla_k \times A_k(k_x, k_y) \tag{3}$$

where $A_k(k_x, k_y) = i\langle u(k)|\nabla_k|u(k)\rangle$ is the Berry connection, with $u(k)$ being the Bloch wave function of the lowest band. The bulk polarization of the lowest band can be calculated as [11]

$$\boldsymbol{P} = -\frac{1}{(2\pi)^2}\int A_k(k_x, k_y)dk_x dk_y. \tag{4}$$

The two components of the bulk polarization can be obtained by a Wilson loop approach [46],

$$P_i = \frac{1}{2\pi}\int v_i(k_j)dk_j, \quad i = x, y, \quad j = y, x, \tag{5}$$

where the integration is carried out over the projection of the first Brillouin zone along k_j, and $v_i(k_j)$ is the Berry phase along the loop k_i for a fixed k_j. Because of the coexistence of time-reversal symmetry and inversion symmetry, the Berry curvature vanishes everywhere for trivial and nontrivial SCs, as shown in Figs. 2(a) and 2(b), respectively. However, the scatter diagrams in Figs. 2(a) and 2(b) indicate the Wannier centers of the trivial SC and the nontrivial SC are different from each other, with 0 for the trivial one and 1/2 for the nontrivial one, which is consistent with the parity analysis at the high-symmetry points in the first Brillouin zone.

Next, the evolutions of bulk polarization with α and Δd are demonstrated in detail. When $\Delta d = 0$ mm, the evolutions of the first band gaps and the corresponding bulk polarization with α are shown in Fig. 2(c). Here, the first band gap is defined by the difference between the lowest frequency of the second band and the highest frequency of the first band, and they are located at X point and M point, respectively, as shown in Fig. 1(c). The absolute band gap forms only when α is located in two ranges: From −164° to −106° and from 16° to 74°, and they own different bulk polarizations. When α deviates from these two ranges, the absolute band gap vanishes [Fig. 2(d)], which can lead to the disappearance of the corner states because they will hybridize with the bulk states. The influences of Δd on bulk polarization when $\alpha = 45°$ and $\alpha = -135°$ are demonstrated in Figs. 2(e) and 2(f), respectively. The distance between neighboring SRRs cannot change the bulk polarization of the SC, but it can change the width and central frequency of the first band gap, which provides a

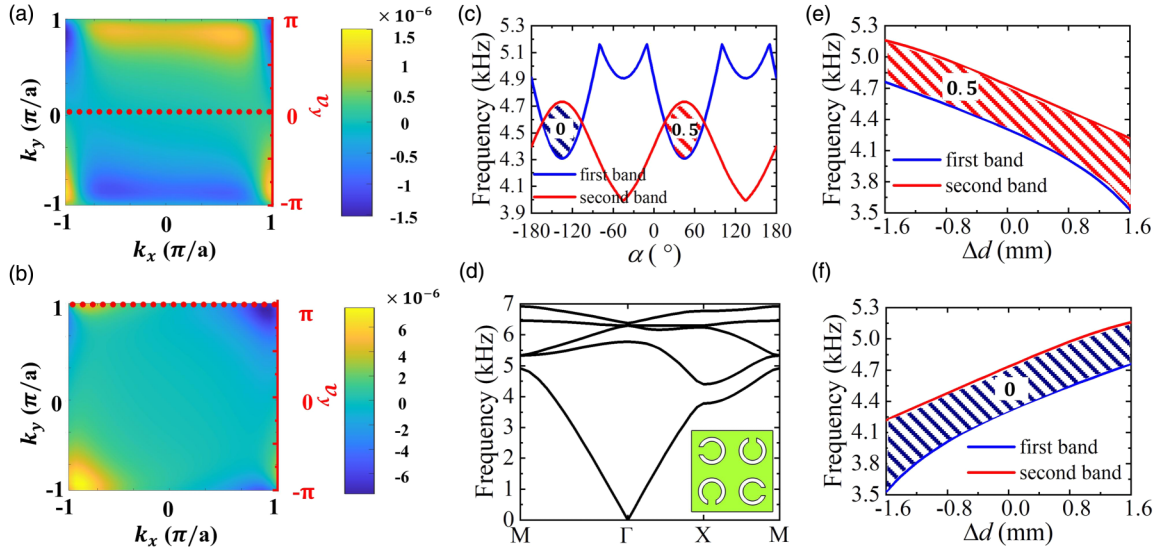

FIG. 2. Demonstration of topological phase transition and frequency tunability. The calculated Berry curvature at the first Brillouin zone and Berry phase v_y as a function of k_x for a trivial SC (a) and a nontrivial SC (b) of the first band. (c) The variation of the first band gap and bulk polarization with the rotational angle α when $\Delta d = 0$. (d) The band structure of the SC when $\alpha = 90°$, where the first band gap disappears. The variation of the first band gap and bulk polarization with the distance of the neighboring SRRs when $\alpha = 45°$ (e) and $\alpha = -135°$ (f).

theoretical basis to tune the frequency of topological corner states.

III. DEMONSTRATION OF ACOUSTIC SOTIs

We construct a box-shaped structure consisting of a $6a^*6a$ nontrivial SC (45, −1.5) surrounded by a trivial SC (−135, 1.5) with a thickness of $5a$ to demonstrate the topological corner states, as shown in Fig. 3(a). The frequencies of eigenstates of this box-shaped structure indicate that the four nearly degenerate corner states appear in the band gap and the edge states appear both in the band gap and below the band gap [see Fig. 3(b)]. These in-gap corner states can also be predicted using the tight-binding model considering the NNN coupling (see Supplemental Material Note S1 [44]). The incomplete degeneracy of these corner states results from the interactions of corner states in different positions. The absolute pressure field profiles of corner states at 4921 Hz, edge states at 4622 Hz, and bulk states at 4249 Hz are demonstrated in Figs. 3(c), 3(d), and 3(e), respectively, which clearly show the different pressure confinement characteristics of these modes.

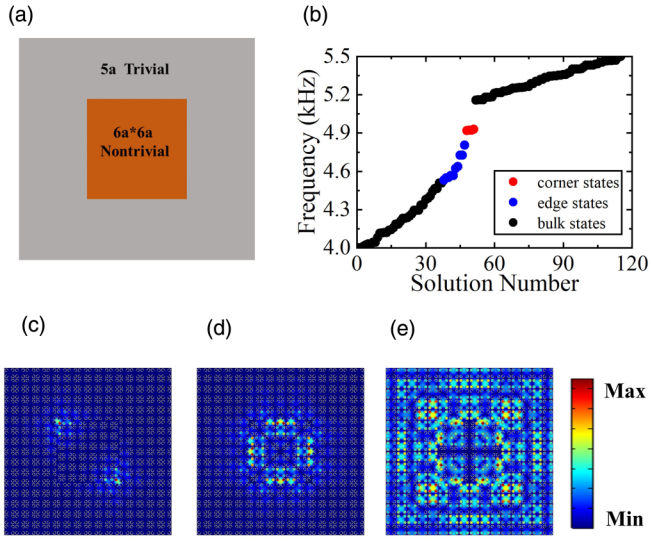

FIG. 3. Observation of topological corner states. (a) Schematic of the box-shaped structure composed of a $6a^*6a$ nontrivial SC surrounded by a trivial SC with a thickness of $5a$. (b) Calculated eigenfrequency distributions of the superstructure. The distribution of absolute pressure field of corner states at 4921 Hz (c), edge states at 4622 Hz (d), and bulk states at 4249 Hz (e).

A discussion on the tunability and robustness against defects of the corner states can be found in Supplemental Material Note S3 [44]. To reveal the pressure distributions of different modes further, the normalized density of states (DOS) [21] of the corner region, edge region, and bulk region are calculated (see Supplemental Material Note S4 for more details [44],) as presented in Fig. 4(a), and the inset demonstrates the chosen regions of corner states, edge states, and bulk states. Note that the partial frequencies of edge states are lower than the lower boundary of the first band gap and mix with bulk states, which can be explained by calculating the band structure of the one-dimensional (1D) ribbon-shaped structure (see Supplemental Material Note S5 [44]).

IV. EXPERIMENTAL VERIFICATION OF TOPOLOGICAL CORNER STATES

To verify experimentally the corner states, edge states, and bulk states, we fabricate a box-shaped structure by photocurable 3D printing and measure the different frequency response of corner detector, edge detector, and bulk detector (experimental setup can be found in Supplemental Material Note S6 [44]). The normalized frequency spectra are demonstrated in Fig. 4(b), which are consistent with the calculated normalized DOS. Note that the measured frequency of corner modes is

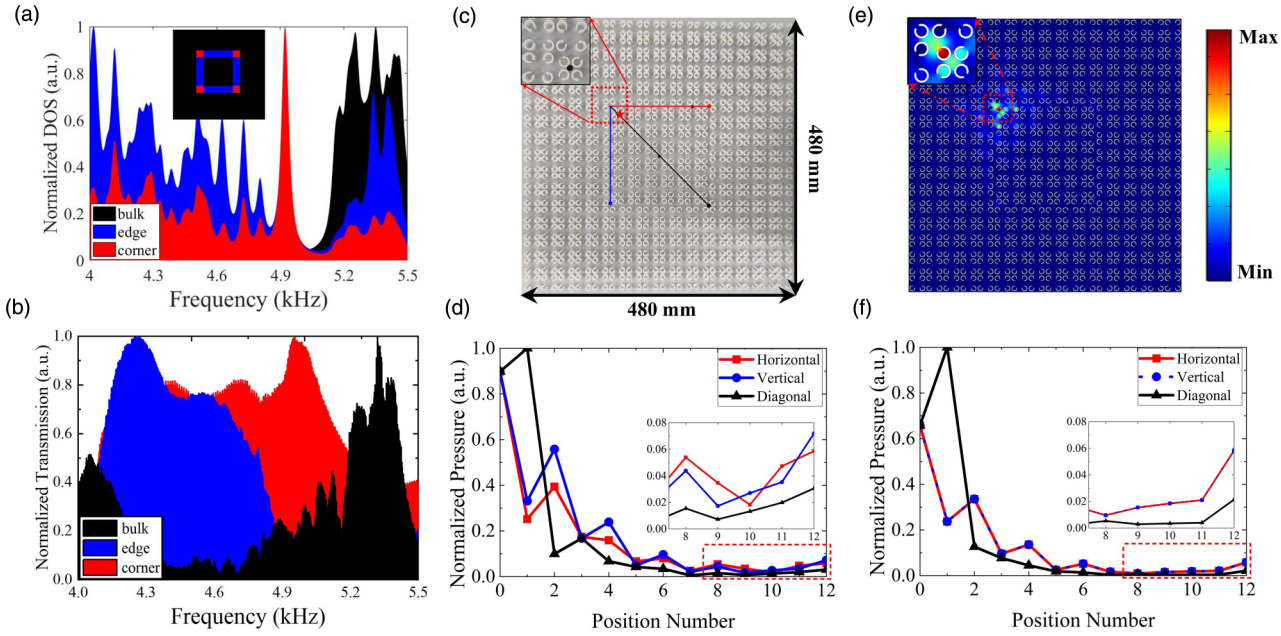

FIG. 4. Experimental validation of topological corner states. (a) Calculated normalized DOS of corner region, edge region, and bulk region. Inset: Schematic of the corner region, edge region, and bulk region. (b) Experimentally measured normalized sound transmission at the corner states, edge states, and bulk states. (c) Photograph of the fabricated sample, with one source (red star) nearing the corner and three different directions for measuring the spatial pressure field distribution of the corner states at 4954 Hz: Red line (horizontal), blue line (vertical), and black line (diagonal). (d) Experimental demonstration of the spatial sound pressure field distribution along three different directions in (c), where 13 detecting points are placed in these three directions with equal spacing. Inset: Enlarged view for detecting points from 8 to 12. (e) Simulated sound pressure profiles for corner states at 4921 Hz. Inset: Enlarged view of the sound pressure profiles in the corner. (f) Measured absolute pressure at some specific points in the simulation are the same as those in the experiment.

located at 4954 Hz with 0.67% deviation, with the calculated one at 4921 Hz, which is caused by the sample's manufacture errors and inevitable environmental losses. However, the measured frequency responses are not able to verify adequately the appearance of corner modes. Here we further measure the spatial sound pressure distributions along with the three directions at 4954 Hz. The experimental setup to measure the corner states is demonstrated in Fig. 4(c), where the source is indicated by a red star, and three different directions to measure the spatial sound pressure are marked by the red, black, and blue lines. The heads (near the source) and ends of these lines are located in the corners, and 13 detecting points with different position numbers are placed in these lines with equal spacing. The measured spatial sound pressure along these three directions is presented in Fig. 4(d). The maximum sound pressure occurs at the corner near the source except for the second point along the diagonal, which is the position of the source. Although the sound pressure decreases overall away from the corner near the source, obvious increases can be found at other corners, as shown in the inset of Fig. 4(d), which indicates that the source can excite all the corner states. The simulated maximum sound pressure occurs at the inner cavity of the SRR located at the corner, as shown in Fig. 4(e), where the velocity of sound in air is $343 + 343 \times 0.01i\,\mathrm{m\,s^{-1}}$ to simulate the lossy environment. However, due to the equivalent size between the inner radius of the SRR and the radius of the 1/4-inch microphones (B&K Type 4958A), we cannot accurately measure the sound pressure of the inner cavity of the SRR. Thus, we only measure the outer sound pressure near the split of the SRR, which is the reason why the measured sound pressure at the corner is lower than that at the source. As shown in Fig. 4(f), the extracted normalized absolute sound pressures in the points that are the same as those in the experiment [see Fig. 4(d)] are consistent with experimental measurements, which further verify the experimental reliability. Note that the sound pressure profiles along the horizontal and those along the vertical are the same in simulation because of the symmetry of the system, as shown in Fig. 4(f). However, they are different in experimental measurements [Fig. 4(d)] due to operational and manufacturing errors.

V. CONCLUSIONS

In conclusion, we have systematically investigated the relationship between a SC consisting of SRRs and the 2D TBM. SRR coupling offers another carrier and flexible methodology to realize the TBM and construct an acoustic SOTI in a realistic physical platform. The direction and distance of the SRRs have an impact on the hoppings, and the topological phase transition can be realized by easily rotating the SRRs. In addition, the frequency can be controlled by translating the SRRs. This SRR system is more convenient to control intercell and intracell hopping than the traditional WRM. To verify the effectiveness of this SRR system, the novel zero Berry phase and bulk polarization have been calculated and the corner states have also been demonstrated in simulation and experiment. Our work may provide more effective methods of constructing the TBM in an acoustic system and may open a new way to design tunable acoustic HOTIs.

ACKNOWLEDGMENTS

This work was financially supported by the National Natural Science Foundation of China (Grants No. 12002258 and No. 51675402), the Natural Science Foundation of Shaanxi Province (Grants No. 2020JQ-043 and No. 2020JQ-074), and the China Postdoctoral Science Foundation–funded project (Grant No. 2022M712540).

[1] W. A. Benalcazar, B. A. Bernevig, and T. L. Hughes, Science **357**, 61 (2017).

[2] W. A. Benalcazar, B. A. Bernevig, and T. L. Hughes, Phys. Rev. B **96**, 245115 (2017).

[3] Z. Song, Z. Fang, and C. Fang, Phys. Rev. Lett. **119**, 246402 (2017).

[4] F. Schindler, A. M. Cook, M. G. Vergniory, Z. Wang, S. S. P. Parkin, B. A. Bernevig, and T. Neupert, Sci. Adv. **4**, eaat0346 (2018).

[5] M. Serra-Garcia, V. Peri, R. Süsstrunk, O. R. Bilal, T. Larsen, L. G. Villanueva, and S. D. Huber, Nature (London) **555**, 342 (2018).

[6] C. W. Peterson, W. A. Benalcazar, T. L. Hughes, and G. Bahl, Nature (London) **555**, 346 (2018).

[7] S. Mittal, V. V. Orre, G. Zhu, M. A. Gorlach, A. Poddubny, and M. Hafezi, Nat. Photon. **13**, 692 (2019).

[8] L. He, Z. Addison, E. J. Mele, and B. Zhen, Nat. Commun. **11**, 3119 (2020).

[9] Y.-J. Qi, C.-Y. Qiu, M. Xiao, H.-L. He, M.-Z. Ke, and Z.-Y. Liu, Phys. Rev. Lett. **124**, 206601 (2020).

[10] M. Ezawa, Phys. Rev. Lett. **120**, 026801 (2018).

[11] H.-R. Xue, Y.-H. Yang, F. Gao, Y.-D. Chong, and B.-L. Zhang, Nat. Mater. **18**, 108 (2019).

[12] X. Ni, M. Weiner, A. Alù, and A. B. Khanikaev, Nat. Mater. **18**, 113 (2019).

[13] Y. Chen, X. Lu, and H. Chen, Opt. Lett. **44**, 4251 (2019).

[14] W. A. Benalcazar and A. Cerjan, Phys. Rev. B **101**, 161116(R) (2020).

[15] Z.-G. Chen, C. Xu, R. Al Jahdali, J. Mei, and Y. Wu, Phys. Rev. B **100**, 075120 (2019).

[16] B. Y. Xie, H. F. Wang, H. X. Wang, X. Y. Zhu, J. H. Jiang, M. H. Lu, and Y. F. Chen, Phys. Rev. B **98**, 205147 (2018).

[17] N. A. Olekhno, A. D. Rozenblit, V. I. Kachin, A. A. Dmitriev, O. I. Burmistrov, P. S. Seregin, D. V. Zhirihin, and M. A. Gorlach, Phys. Rev. B **105**, L081107 (2022).

[18] A. Cerjan, M. Jurgensen, W. A. Benalcazar, S. Mukherjee, and M. C. Rechtsman, Phys. Rev. Lett. **125**, 213901 (2020).

[19] Z.-W. Zhang, H.-Y. Long, C. Liu, C. Shao, Y. Cheng, X.-J. Liu, and J. Christensen, Adv. Mater. **31**, 1904682 (2019).

[20] X.-J. Zhang, H.-X. Wang, Z.-K. Lin, Y. Tian, B.-Y. Xie, M.-H. Lu, Y.-F. Chen, and J.-H. Jiang, Nat. Phys. **15**, 582 (2019).

[21] X.-J. Zhang, Z.-K. Lin, H.-X. Wang, Z. Xiong, Y. Tian, M.-H. Lu, Y.-F. Chen, and J.-H. Jiang, Nat. Commun. **11**, 65 (2020).

[22] X.-J. Zhang, L. Liu, M.-H. Lu, and Y.-F. Chen, Phys. Rev. Lett. **126**, 156401 (2021).

[23] X.-X. Wu, Y. Meng, Y.-R. Hao, R.-Y. Zhang, J. Li, and X. Zhang, Phys. Rev. Lett. **126**, 226802 (2021).

[24] W.-P. Su, J. R. Schrieffer, and A. J. Heeger, Phys. Rev. Lett. **42**, 1698 (1979).

[25] E. J. Meier, F. A. An, and B. Gadway, Nat. Commun. **7**, 13986 (2016).

[26] M. Yan, X.-Q. Huang, L. Luo, J.-Y. Lu, W.-Y. Deng, and Z.-Y. Liu, Phys. Rev. B **102**, 180102(R) (2020).

[27] B.-Y. Xie, G.-X. Su, H.-F. Wang, H. Su, X.-P. Shen, P. Zhan, M.-H. Lu, Z.-L. Wang, and Y.-F. Chen, Phys. Rev. Lett. **122**, 233903 (2019).

[28] X.-D. Chen, W.-M. Deng, F.-L. Shi, F.-L. Zhao, M. Chen, and J.-W. Dong, Phys. Rev. Lett. **122**, 233902 (2019).

[29] Z. Zhang, M. Rosendo López, Y. Cheng, X. Liu, and J. Christensen, Phys. Rev. Lett. **122**, 195501 (2019).

[30] M. R. López, Z.-W. Zhang, D. Torrent, and J. Christensen, Commun. Phys. **2**, 132 (2019).

[31] Z.-G. Chen, L.-C. Wang, G.-Q. Zhang, and G.-C. Ma, Phys. Rev. Appl. **14**, 024023 (2020).

[32] Z.-G. Chen, W. Zhu, Y. Tan, L. Wang, and G. Ma, Phys. Rev. X **11**, 011016 (2021).

[33] H.-R. Xue, Y.-H. Yang, G.-G. Liu, F. Gao, Y.-D. Chong, and B.-L. Zhang, Phys. Rev. Lett. **122**, 244301 (2019).

[34] S.-J. Zheng, B.-Z. Xia, X.-F. Man, L. Tong, J.-R. Jiao, G.-J. Duan, and D.-J. Yu, Phys. Rev. B **102**, 104113 (2020).

[35] J. B. Pendry, A. J. Holden, D. J. Robbins, and W. J. Stewart, IEEE Trans. Microwave Theory Tech. **47**, 2075 (1999).

[36] D. R. Smith, W. J. Padilla, D. C. Vier, S. C. Nemat-Nasser, and S. Schultz, Phys. Rev. Lett. **84**, 4184 (2000).

[37] H. O. Moser, B. D. F. Casse, O. Wilhelmi, and B. T. Saw, Phys. Rev. Lett. **94**, 063901 (2005).

[38] A. B. Movchan and S. Guenneau, Phys. Rev. B **70**, 125116 (2004).

[39] D. P. Elford, L. Chalmers, F. V. Kusmartsev, and G. M. Swallowe, J. Acoust. Soc. Am. **130**, 2746 (2011).

[40] J. Jiang, Z. W. Guo, Y. Q. Ding, Y. Sun, Y. H. Li, H. T. Jiang, and H. Chen, Opt. Express **26**, 12891 (2018).

[41] A. Krynkin, O. Umnova, A. Y. B. Chong, S. Taherzadeh, and K. Attenborough, J. Phys. D Appl. Phys. **44**, 125501 (2011).

[42] G. Dupont, F. Remy, O. Kimmoun, B. Molin, S. Guenneau, and S. Enoch, Phys. Rev. B **96**, 180302(R) (2017).

[43] F. Liu and K. Wakabayashi, Phys. Rev. Lett. **118**, 076803 (2017).

[44] See Supplemental Material at http://link.aps.org/supplemental/10.1103/PhysRevB.106.045403 for tight-binding model analysis of the SRRs system, eigenstates of the trivial and nontrivial SC, the tunability and robustness against defects of the corner states, the details for calculating the normalized DOS, the band structure of the 1D ribbon-shaped structure, and the experimental setup to calculate the normalized sound transmission of corner states, edge states, and bulk states.

[45] C. Fang, M. J. Gilbert, and B. A. Bernevig, Phys. Rev. B **86**, 115112 (2012).

[46] H. Wang, G. Guo, and J. Jiang, New J. Phys. **21**, 093029 (2019).